Journal of Alloys and Compounds 1020 (2025) 179470

Contents lists available at ScienceDirect

Journal of Alloys and Compounds

journal homepage: www.elsevier.com/locate/jalcom

# High-pressure high-temperature melting and recrystallization of nanolamellar high-entropy alloys

Kallol Chakrabarty [a,*], Andrew D. Pope [a], Abhinav Yadav [b], Wuxian Yang [c], Jie Ren [c], Vijaya Rangari [b], Wen Chen [c], Yogesh K. Vohra [a]

[a] Department of Physics, University of Alabama at Birmingham, AL 35294, USA
[b] Department of Materials Science and Engineering, Tuskegee University, AL 36088, USA
[c] Department of Mechanical and Industrial Engineering, University of Massachusetts, Amherst, MA 01003-2210, USA

ARTICLE INFO

*Keywords:*
Additively manufactured
Laser powder bed fusion
High Entropy Alloy
High-pressure high-temperature
Energy dispersive X-ray diffraction
Memory retention

ABSTRACT

Additively manufactured (AM) High Entropy Alloys (HEAs) are notable for their exceptional high-yield strength and large tensile ductility. The nanolamellar Eutectic HEA (EHEA) $AlCoCrFeNi_{2.1}$ was fabricated by laser powder bed fusion (L-PBF) in the as-printed form (EHEA1) and subsequently annealed at 1000 °C (EHEA2) and 600 °C (EHEA3) to achieve a broad range of mechanical properties. EHEA2 and EHEA3 samples were studied using Scanning transmission electron microscopy (STEM), energy dispersive X-ray diffraction (EDXRD) at high-pressures and high temperatures, nanoindentation hardness and modulus measurements. According to EDXRD EHEA2 and EHEA3 are composed of B2 and $L1_2$ phases. High-pressure high-temperature EDXRD studies show melting for EHEA2 at 1698 ± 25 K at a pressure of 6.5 GPa and melting for EHEA3 at 1598 ± 25 K at a pressure of 5.8 GPa. Post-melt and recrystallized samples were recovered at ambient conditions, and XRD analysis showed retention of B2 and $L1_2$ phases, although a new σ phase appeared for both EHEA2 and EHEA3 samples due to high-pressure and high-temperature melting and recrystallization experiment. SEM analysis also demonstrated the preservation of the nanolamellar morphology. Nanoindentation studies revealed that recrystallized EHEAs retain their original mechanical property hierarchy, with EHEA3 being 47 % harder than EHEA2, largely related to higher content of B2-phase and retention of nanolamellar morphology. We also present Pressure-Volume-Temperature (P-V-T) data for 3-D printed and annealed eutectic high entropy alloys and extract mechanical and thermal properties data.

## 1. Introduction

High-entropy alloys (HEA) are a class of alloys in which five or more principal elements are alloyed, and the entropy of mixing is lower than the enthalpy of formations. [1,2]. Gibb's free energy of the mixing can be expressed as the following Eq. (1),

$$\Delta_{mix}G = \Delta_{mix}H - T\Delta_{mix}S \quad (1)$$

Gibbs free energy would then result in enthalpy of formation ($\Delta_{mix}H$) near zero and a dominating entropy of mixing ($\Delta_{mix}S$) term forming an alloy with atoms randomly assorted throughout its bulk [1–3]. So far, these alloys tend to be simple in structure as they commonly take on a face-centered cubic (FCC), body-centered cubic (BCC), or hexagonal closed-packed (HCP) structure driven by the high-entropy effect [4]. Significant advancements have been made in developing HEA, exhibiting exceptional properties in recent years. These alloys are characterized by unique performances such as high strength, excellent corrosion resistance, and high plasticity. These remarkable properties can be attributed to the four fundamental "core effects" of HEA: the high entropy effect, which stabilizes the solid solution phase; the lattice distortion effect, which strengthens the material by impeding dislocation movement; the sluggish diffusion effect, which enhances thermal stability; and the cocktail effect, which arises from the synergistic combination of multiple elements, leading to improved properties [5–9]. Among HEAs, eutectic high entropy alloys are a dual-phase FCC/BCC bulk structure that incorporates the principles of eutectic systems, where two or more phases solidify simultaneously at a specific composition and temperature [4]. As pioneers in the field of eutectic alloy research, Liao and Baker developed the $Fe_{30}Ni_{20}Mn_{35}Al_{15}$ eutectic alloy, extensively investigating its microstructure and mechanical

* Corresponding author.
*E-mail address:* kallol89@uab.edu (K. Chakrabarty).

https://doi.org/10.1016/j.jallcom.2025.179470
Received 21 November 2024; Received in revised form 23 February 2025; Accepted 25 February 2025
Available online 26 February 2025

properties [10–13]. Their work laid the foundation for understanding the design principles of eutectic high entropy alloys (EHEAs) and their potential applications. Lu et al. later advanced this concept by proposing the EHEA design strategy and successfully synthesizing the well-known $AlCoCrFeNi_{2.1}$alloy, which has since become a model system for EHEA research [13–15]. This breakthrough marked a paradigm shift in high-entropy alloy (HEA) development, moving beyond the traditional approach primarily focused on single-phase solid solutions to a composite-like strategy that balances strength and ductility through multiphase design [13,14]. The eutectic microstructure of $AlCoCrFeNi_{2.1}$ consists of a well-ordered FCC phase ($L1_2$) and an ordered BCC phase (B2), forming a finely tuned lamellar structure [13,14]. Unlike conventional HEAs, where phase stability and solid-solution strengthening dominate the design philosophy, the composite-like approach in EHEAs allows for the simultaneous optimization of mechanical properties by tailoring the volume fraction and distribution of the eutectic phases. This enables EHEAs to achieve a unique combination of high strength and good ductility, overcoming the brittleness often associated with single-phase HEAs [13,14]. EHEA utilizes both the strength of a BCC phase and ductility of an FCC phase through refined nano-lamella structure, which makes them desirable in industrial applications [4, 16,17]. This microstructural refinement enhances the mechanical properties of EHEAs, making them ideal candidates for applications requiring materials with high strength and toughness [14,18,19]. EHEAs are designed to maintain their structural integrity under thermal stress, showcasing significant microstructural stability. A study highlighted that such alloys can retain their dual-phase characteristics, which is paramount for applications exposed to high temperatures [20]. The stability of these alloys is influenced by several factors, including processing conditions, cooling rates, and thermal treatment protocols that determine their phase evolution [21]. Additionally, recent research emphasizes the importance of microstructural evolution during thermal cycling, suggesting that carefully managed thermal treatments can effectively maintain phase integrity [13]. This microstructural refinement enhances the mechanical properties of EHEAs, making them ideal candidates for applications requiring materials with high strength and toughness [14,18,19]. One of the most compelling aspects of EHEAs is their potential for use in extreme environments, such as high temperatures and pressures [21]. Maintaining structural integrity and performance under such conditions is critical for aerospace, automotive, and energy applications.

Additive manufacturing has revolutionized the field of materials synthesis, offering unprecedented opportunities for the design and fabrication of complex structures with tailored properties [22–25]. The advent of laser powder-bed fusion has further expanded the potential of EHEAs by additive manufacturing [26,27]. This process allows for the precise control of the alloy's microstructure and facilitates the fabrication of complex geometries that are difficult to achieve through traditional manufacturing methods. The rapid solidification rates inherent in L-PBF promote the formation of fine nanostructures and far-from-equilibrium phases, which can enhance the mechanical properties of the resulting material. For instance, Katagiri et al. recently investigated the static and shock compression behavior of the as printed EHEA $AlCoCrFeNi_{2.1}$ (EHEA1) [28]. The process in which these EHEAs were produced, has extremely high cooling rates ($10^7$ K/s) and allows the material to rapidly cool through its eutectic point, creating unique microstructures that have proven to be beyond those of conventionally produced EHEAs. [16] In conventional processing methods, the thickness of the lamellae typically falls within the micrometer or sub-micrometer range, whereas the additively manufactured (AM) $AlCoCrFeNi_{2.1}$ sample has a nanometer-scale lamellae thickness. Several studies have explored the microstructural evolution, phase stability, and mechanical performance of EHEAs under various processing conditions [20,21]. Previous research has demonstrated the influence of solidification pathways, phase transformations, and thermomechanical treatments on the hierarchical microstructures and mechanical properties of these alloys. However, limited attention has been given to the behavior of EHEAs under high-pressure, high-temperature (HPHT) conditions, particularly regarding their melting, recrystallization, and subsequent microstructural retention.

The objective of this study is to investigate the effects of high-pressure and high-temperature (HPHT) conditions on the structural, mechanical, and microstructural properties of the Eutectic High Entropy Alloy (EHEA). $AlCoCrFeNi_{2.1}$ samples were synthesized using Laser Powder Bed Fusion (L-PBF) and then annealed under two distinct conditions: at 1000°C for one hour (EHEA2) and at 600°C for five hours (EHEA3). Understanding the behavior of HEAs under HPHT conditions is essential for their application in environments that demand high structural integrity and reliability. Such conditions can cause significant changes in the microstructure and mechanical properties of the alloys, affecting their performance and longevity. Therefore, it is crucial to investigate the memory retention capabilities of these materials following exposure to HPHT conditions. Memory retention, in this context, refers to the ability of the alloy to retain its phase, mechanical properties, and microstructural characteristics after melting and subsequent recrystallization. During the high-pressure and high-temperature study, EHEA2 and EHEA3 were melted within a Paris-Edinburgh (PE) cell and allowed to recrystallize. The crystalline structure of the recrystallized EHEA2 and EHEA3 samples were analyzed using X-ray diffraction and mechanical properties by nanoindentation, and their morphology was examined through scanning electron microscopy (SEM).

## 2. Materials and methods

$AlCoCrFeNi_{2.1}$ samples were additively manufactured using M290 (EOS) Laser powder bed fusion with an ytterbium-fiber laser whose max power was 400 W and had a focal diameter of 100μm. One of the $AlCoCrFeNi_{2.1}$ samples was annealed at 1000 °C for an hour (labeled as EHEA2) and the other 600 °C for five hours (labeled as EHEA3). High-Angle Annular Dark-Field Scanning TEM (HAADF-STEM) was conducted using an FEI Titan S/TEM operating at 300 keV to investigate elemental composition of the BCC and FCC phases through Energy Dispersive X-ray Spectroscopy (EDX) analyses. Energy dispersive x-ray diffraction was carried out at the Advanced Photon Source at Argonne National Lab sector and beamline 16-BM-B which host the Paris-Edinburgh (PE) press. The $AlCoCrFeNi_{2.1}$ cylindrical sample was loaded into a MgO chamber that matched the dimensions of the cylinder. A MgO chamber was placed in a graphite shell followed by a zirconia disk and latex outer ring. Zirconia was loaded above and below that contained a Ta rod on which a silver paste was applied, and Ta foil was placed on to ensure electrical conductivity between the PE press and cell. The current was applied through the Ta foil, where resistive heating from the graphite shell up to 1723 K was achieved. The pressure was brought to 5 GPa, where it was held, and the temperature was increased in steps of 50 K. The pressure in the cell is maintained via a hydraulic press and the sample pressure is calibrated by the measured volume of MgO included in the sample assembly [29]. The temperature is calibrated by the power supplied to a graphite heater enclosing the sample assembly. The pressure was increased in steps of 3000 psi up to 12, 000 psi with an intermediate temperature ramp. The temperature was ramped in steps of $100^0$ C up to $1200^0$ C (before melting), where it was ramped until melting at the highest-pressure step. The direct ramp rates are not monitored, but the temperature is through the resistive heating process as it is a function of the delivered power. The pressure stability is held within a few psi through a feedback loop created by HPCAT. Energy dispersive x-ray diffraction spectrums were taken at wavelength 1.54051 Å held at an angle of $2\theta = 5^\circ$ degrees over an energy range of 5–130 keV. Peak fitting and background subtraction were conducted with GSAS-II [30] and the thermal equation of state fitting was performed with EoSFit7 [31]. During the high-pressure, high-temperature study, EHEA2 and EHEA3 samples were melted and recrystallized inside

the PE cell. The recrystallized samples were then collected for further analysis. The sample nomenclature is provided in Table 1.

In our previous work, we conducted a comprehensive study on as-printed $AlCoCrFeNi_{2.1}$ eutectic high-entropy alloys (EHEAs) and those annealed at various temperatures. Among the samples studied, it was observed that the sample annealed at 600°C (EHEA3) exhibited the highest strength, while the sample annealed at 1000°C (EHEA2) demonstrated the greatest ductility [16]. These findings highlight a trade-off between strength and ductility, with the annealing temperature playing a critical role in tailoring the mechanical properties of EHEAs. Based on these results, the EHEA3 (600°C) and EHEA2 (1000°C) samples were selected for the current study to further explore their behavior under high-pressure and high-temperature (HPHT) conditions.

For X-ray diffraction (XRD) analysis of EHEA2 * and EHEA3 * , a Panalytical Empyrean X-ray diffractometer with Copper Kα radiation (λ = 1.54059 Å) was utilized. Nanoindentation hardness was measured using an Agilent Nano Indenter G200, utilizing the continuous stiffness measurement (CSM) technique. This setup was equipped with a Berkovich diamond tip characterized by a nominal radius of 50 nm. To ensure high precision and reliability of the measurements, calibration was performed using a fused silica reference standard, which possesses a well-established Young's modulus of 72 ± 3 GPa. Calibration involved conducting indentations on the silica reference before and after testing the sample. The consistent Young's modulus values recorded from the silica standard, both before and following the sample indentation, affirmed the preservation of the tip geometry throughout the entire testing process. All indentations, including the silica reference and EHEA2 * and EHEA3 * samples, were carried out with a maximum indentation depth of 750 nm. The EHEA2 * and EHE3 * samples microstructures were analyzed using a JEOL JSM-7200F field emission scanning electron microscope (FESEM, JEOL USA, Peabody, MA).

## 3. Results

### 3.1. STEM-EDS analysis

Fig. 1 shows all samples exhibit the Al, Ni-rich BCC phase (dark region) and Cr, Co, Fe-rich FCC phase (bright region). However, the elemental segregation in the EHEA1 sample is less obvious compared to the annealed samples EHEA2 and EHEA3. The Cr-rich nanoprecipitates are observed in both EHEA2 and EHEA3. For the EHEA3 sample, the nanoprecipitates accumulate in clusters and are heterogeneously distributed in the BCC and FCC phases, while for the EHEA2, the relatively uniform distribution of nanoprecipitates is mainly observed in the BCC phase. For the EHEA2 sample, lamellae coarsening and degradation-induced heterogenous bi-modal lamellae structures are evident.

### 3.2. Ex-situ neutron diffraction

Fig. 2 displays the ex-situ neutron diffraction patterns of the as-printed, EHEA3 and EHEA2 samples. All three samples exhibit a broad range of peaks and consist of BCC and FCC phases, as determined through Rietveld refinement. Additionally, the EHEA2 sample, annealed at 1000°C for 1 hour, exhibits a small ordered B2 peak.

**Table 1**
EHEA sample nomenclature.

| Sample Name | Property |
|---|---|
| EHEA1 | As printed $AlCoCrFeNi_{2.1}$ sample |
| EHEA2 | As printed $AlCoCrFeNi_{2.1}$ sample annealed at 1000 °C for an hour |
| EHEA3 | As printed $AlCoCrFeNi_{2.1}$ sample annealed at 600 °C for five hour |
| EHEA2 * | Melted and recrystallized EHEA2 sample |
| EHEA3 * | Melted and recrystallized EHEA3 sample |

### 3.3. High-pressure high-temperature study

Fig. 3(a) showcases the results of our high-pressure, high-temperature EDXRD study of the EHEA2 sample carried out at 6.5 GPa and 1673 K. The dual-phase structure of $L1_2$ (FCC) and B2 (BCC) is identifiable from the diffraction peaks. The $L1_2$ (FCC) phase is indicated by the (111), (200), (220), (311), and (222) peaks, shown in blue. Meanwhile, the B2 (BCC) phase is represented by the (100), (110), (200), and (211) peaks, shown in red. These peaks confirm the presence of a stable BCC-FCC dual-phase mixture up to 1673 K at 6.5 GPa, demonstrating the robustness of this dual-phase structure under high-pressure and high-temperature conditions. As the temperature increases to 1723 K, Fig. 3 (b) reveals that all crystalline diffraction peaks disappear. This results in a diffraction pattern characterized by the disappearance of the distinct crystalline peaks and the emergence of a broad, amorphous pattern indicative of the liquid state. Similarly, Fig. 3(c) presents the results of our high-pressure, high-temperature EDXRD study of EHEA3 conducted at 5.8 GPa and 1573 K. The existence of the dual FCC/BCC structure can be seen from the (111), (200), (220), (311), and (222) peaks in blue representing the $L1_2$ (FCC) phase and (100), (110), (200), and (211) peaks in red representing the B2 (BCC) phase. The BCC-FCC dual-phase mixture remains stable until temperature 1573 K at 5.8 GPa. Upon further heating to 1623 K, all crystalline diffraction peaks of EHEA3 disappear, resulting in an amorphous diffraction pattern shown in Fig. 3 (d).

We also present the Pressure-Volume-Temperature (P-V-T) data for EHEA2 and EHEA 3 in the supplementary documentation (Figure S1). The P-V-T is fitted to extract the bulk modulus, derivative of bulk modulus, thermal expansion alpha parameters, and derivative of bulk modulus with respect to temperature values for the FCC and BCC phases of EHEA2 and EHEA3 (Table S1).

### 3.4. X-ray diffraction analysis

Fig. 4 presents the XRD patterns of EHEA2 * and EHEA3 * after melting under static high-pressure and high-temperature conditions. Rietveld refinement revealed a mixed-phase structure consisting of B2, $L1_2$, and σ phases in EHEA2 * and EHEA3 * . EHEA 2 * consists of 32 % B2, 62 % $L1_2$, and 6 % σ phases, whereas EHEA 3 * consists of 40 % B2, 54 % $L1_2$, and 6 % σ phases. The B2 phase is an ordered variant of the BCC crystal structure, and the $L1_2$ phase has an FCC crystal structure, but unlike a regular FCC structure, it has a specific ordering of different types of atoms. According to EDXRD analysis, no additional peaks corresponding to other phases except BCC and FCC were detected. The appearance of the σ phase in XRD likely results from the recrystallization process following melting. The lattice parameters of B2, $L1_2$, and σ phases of EHEA2 * and EHEA3 * samples were measured using GSAS-II and listed in Table 2. As EHEAs are compositionally complex materials, NiAl was used to refine the B2 phase [32], $Ni_3Al$ was used to refine the $L1_2$ phase [33], and FeCr was used to refine the σ-phase [34].

### 3.5. Scanning electron microscopy (SEM) analysis

Fig. 5 presents scanning electron microscopy (SEM) of the nanolamellar structure of the EHEA 2 * and EHEA 3 * samples. The morphology highlights the pattern of alternating nanolayers characterized by B2 (BCC) and $L1_2$ (FCC) phases. The SEM images were obtained following the recrystallization process conducted under high-pressure and high-temperature conditions within a PE cell. According to the previous study, the dark region is the B2 phase, and the bright area is the $L1_2$ phase [16]. The small amount of σ phase generally resides at the interface between the B2 and $L1_2$ phases.

### 3.6. Nanoindentation hardness and Young's modulus

Nanoindentation hardness values for EHEA2 * and EHEA3 * alloys

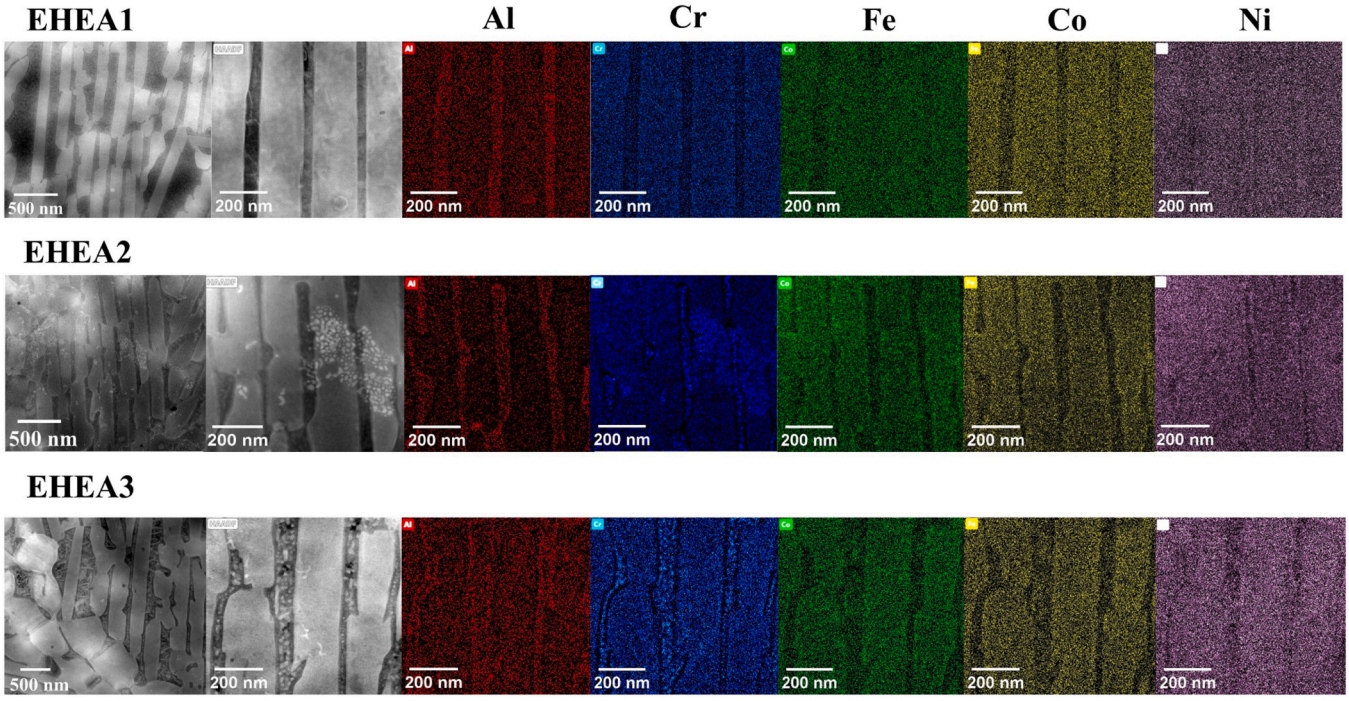


**Fig. 1.** STEM-EDS elemental mappings of the EHEA1, EHEA2 and EHEA3 samples. EHEA1, EHEA2 and EHEA3 samples revealed nanolamellar structure.

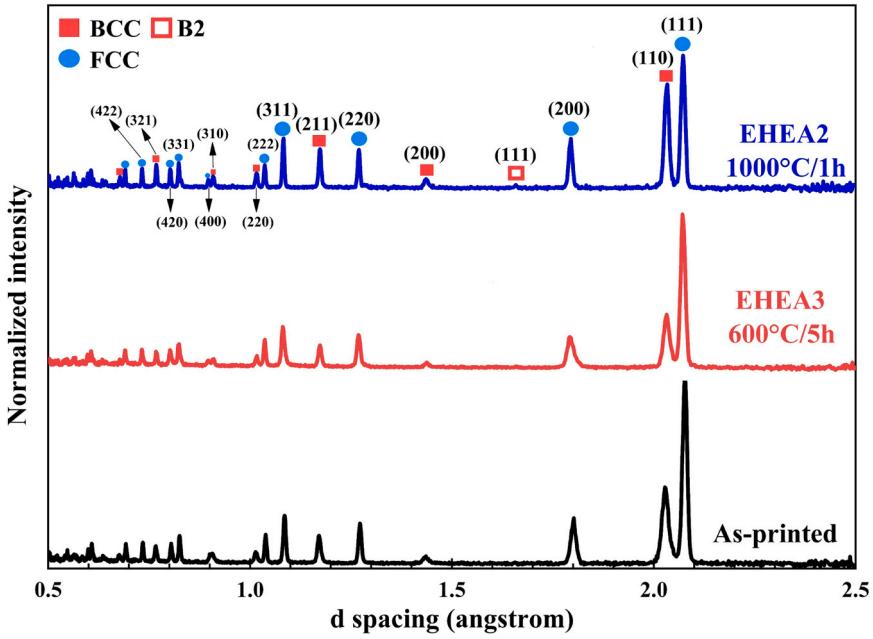


**Fig. 2.** Ex situ neutron diffraction of, as printed, EHEA3, and EHEA2 samples. All the three samples have both BCC and FCC phases.

were measured across a depth range of 100–700 nm, demonstrating consistent hardness properties within this range. EHEA2 * exhibited an average hardness of 4.9 GPa with a standard deviation of 0.2 GPa, while EHEA3 * showed a hardness of 7.2 GPa with a standard deviation of 0.3 GPa. Figs. 6(a) and 6(b) depict the nanoindentation hardness values of EHEA2 * and EHEA3 * , plotted against displacement into the surface, illustrating the relationship between depth and hardness. For Both EHEA2 * and EHEA3 * , hardness remained consistent across all depths and highlighting the material's uniform hardness characteristics. In addition to hardness measurements, Young's modulus of elasticity was evaluated within the same depth range of 100–700 nm, revealing minimal variation across these depths. EHEA2 * displayed a mean Young's modulus of 194.6 GPa with a standard deviation of 7.2 GPa, shown in Fig. 6(c), whereas EHEA3 * exhibited a mean Young's modulus of 211.2 GPa with a standard deviation of 6 GPa, shown in Fig. 6(d). This uniformity in modulus values across the depth range suggests the consistent elastic properties of both alloys throughout the measured depth. The nanoindentation load vs. displacement curve is also presented in supplementary data. We have also calculated the confidence intervals and the coefficient of variation of the hardness and modulus data and added them to the supplementary data section.

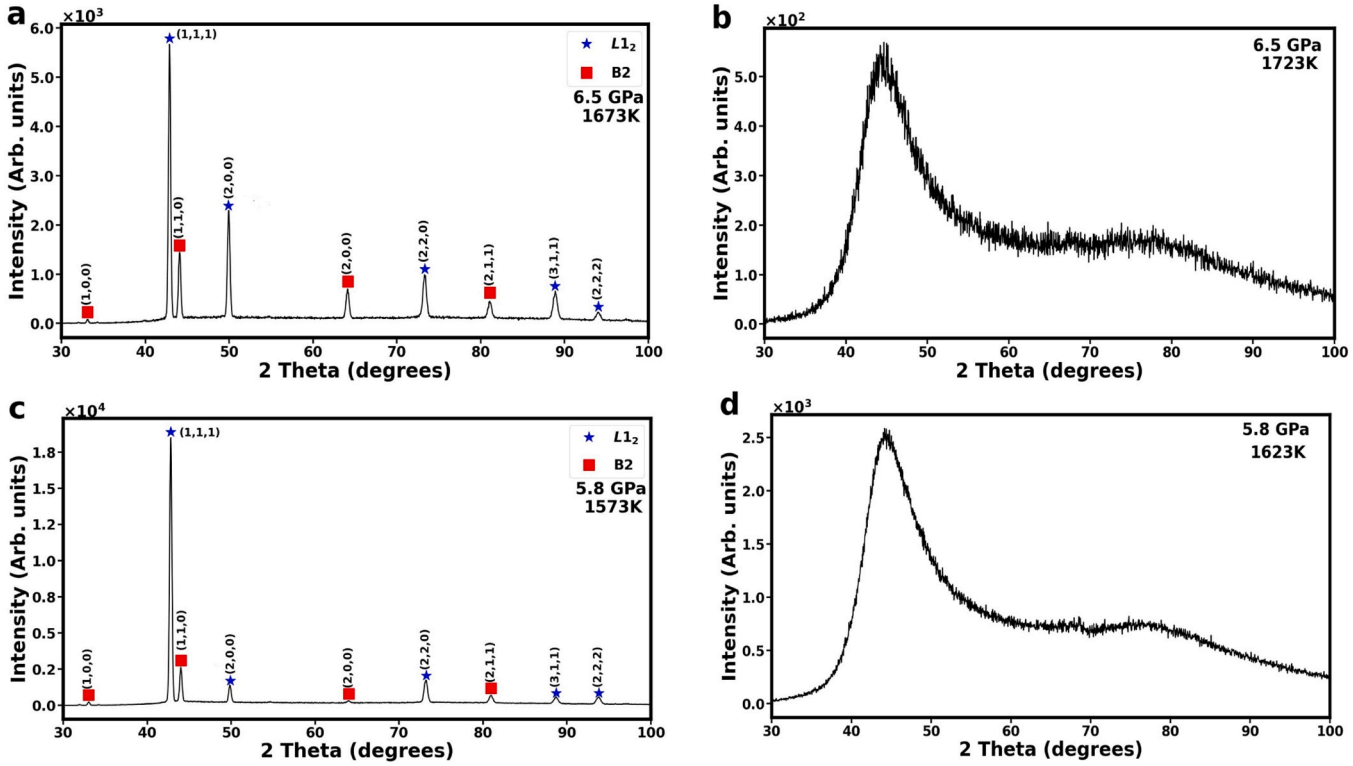


**Fig. 3.** Energy dispersive X-ray Diffraction (EDXRD) and melt spectrum of EHEA2 and EHEA3. **(a)** EDXRD on the EHEA2 at the highest pressure and temperature of 6.5 GPa and 1723 K. $L1_2$ (FCC) is labeled through blue stars; B2 (BCC) is labeled through red squares; **(b)** Melt spectrum of the EHEA2; **(c)** EDXRD on the EHEA3 at the highest pressure and temperature of 5.8 GPa and 1623 K. $L1_2$ (FCC) is labeled through blue stars; B2 (BCC) is labeled through red squares; **(d)** Melt spectrum of the EHEA3.

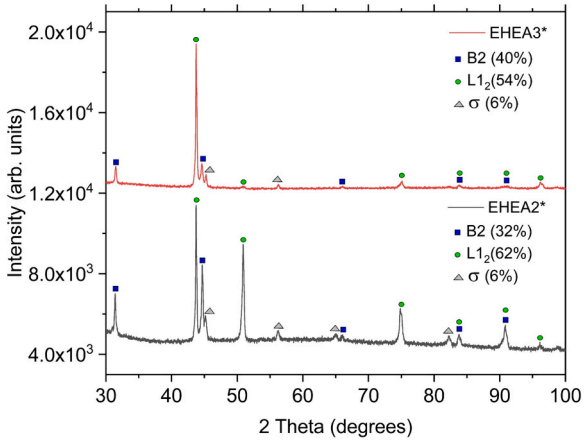


**Fig. 4.** X- ray diffraction pattern of EHEA2 * and EHEA3 * samples at ambient conditions, following melting under static high pressure and high temperature, shows the presence of B2, $L1_2$, and σ phases in both samples.

## 4. Discussion

The analysis conducted via high-pressure, high-temperature EDXRD before recrystallization of the samples confirmed the coexistence of both B2 (BCC) and $L1_2$ (FCC) phases within the alloys. Remarkably, following the recrystallization process, both EHEA2 * and EHEA3 * preserved their structural integrity, evidenced by the sustained presence of B2 (BCC) and $L1_2$ (FCC) phases, as validated by X-ray diffraction (XRD) and SEM analyses. Previous work on the as printed EHEA $AlCoCrFeNi_{2.1}$ samples revealed dual-phase nano lamellae consisting of alternating body-centered cubic (BCC) and face-centered cubic (FCC) nanolayers [16]. Our current work also demonstrates that EHEA2 and EHEA3 samples have nanolamellar structures according to STEM analysis, and recrystallized EHEA2 * and EHEA3 * samples also retain the nano-lamellar structure. According to EDXRD, the sample became amorphous during the melting process. After recrystallization, it retained the memory, and B2(BCC) and $L1_2$ (FCC) phases appeared along with the nanolamellar structure. This observation underscores the stability of these additively manufactured eutectic high-entropy alloys under extreme operational conditions, thereby establishing them as promising candidates for applications that demand materials with outstanding structural properties.

**Table 2**
Summary of Lattice parameters from the present work and other references.

| Sample | Phase | Lattice parameter | | Unit Cell Volume (Å)$^3$ |
|---|---|---|---|---|
| | | a (Å) | c(Å) | |
| EHEA2 * | B2 | 2.8387 | 2.8387 | 22.874 |
| | $L1_2$ | 3.5846 | 3.5846 | 46.049 |
| | σ | 8.7945 | 4.5513 | 352.013 |
| EHEA3 * | B2 | 2.8301 | 2.8301 | 22.669 |
| | $L1_2$ | 3.5810 | 3.5810 | 45.923 |
| | σ | 8.7998 | 4.5449 | 351.940 |
| NiAl [32] | B2 | 2.8597 | 2.8597 | 23.387 |
| $Ni_3Al$ [33] | $L1_2$ | 3.5231 | 3.5231 | 43.728 |
| FeCr [34] | σ | 8.8 | 4.544 | 351.887 |

The mechanical properties of eutectic high-entropy alloys (EHEAs) are intricately linked to their microstructural composition, with specific phases playing crucial roles in determining strength and ductility. The body-centered cubic (BCC) phase is predominantly responsible for the strength characteristics of these alloys, while the face-centered cubic (FCC) phase imparts inherent ductility. Through X-ray diffraction (XRD) analysis, we have identified EHEA3 * and EHEA2 * have B2, $L1_2$ and

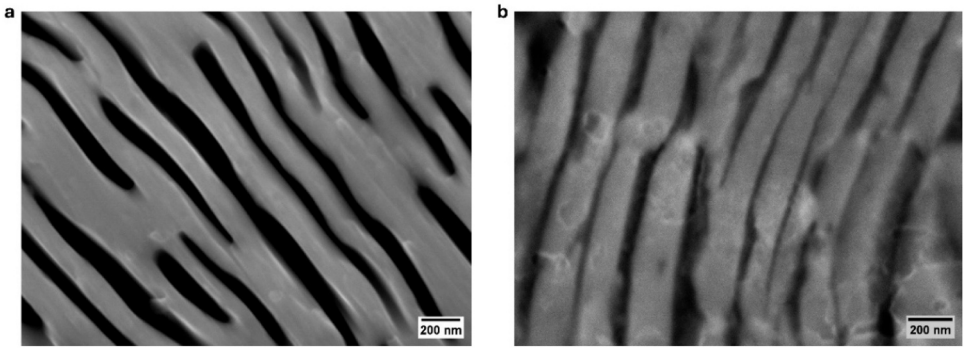


**Fig. 5.** Scanning electron microscopy (SEM) reveals (a) EHEA2 * and **(b)** EHEA3 * consisting of alternating nanolayers of B2(BCC) and $L1_2$ (FCC) structures.

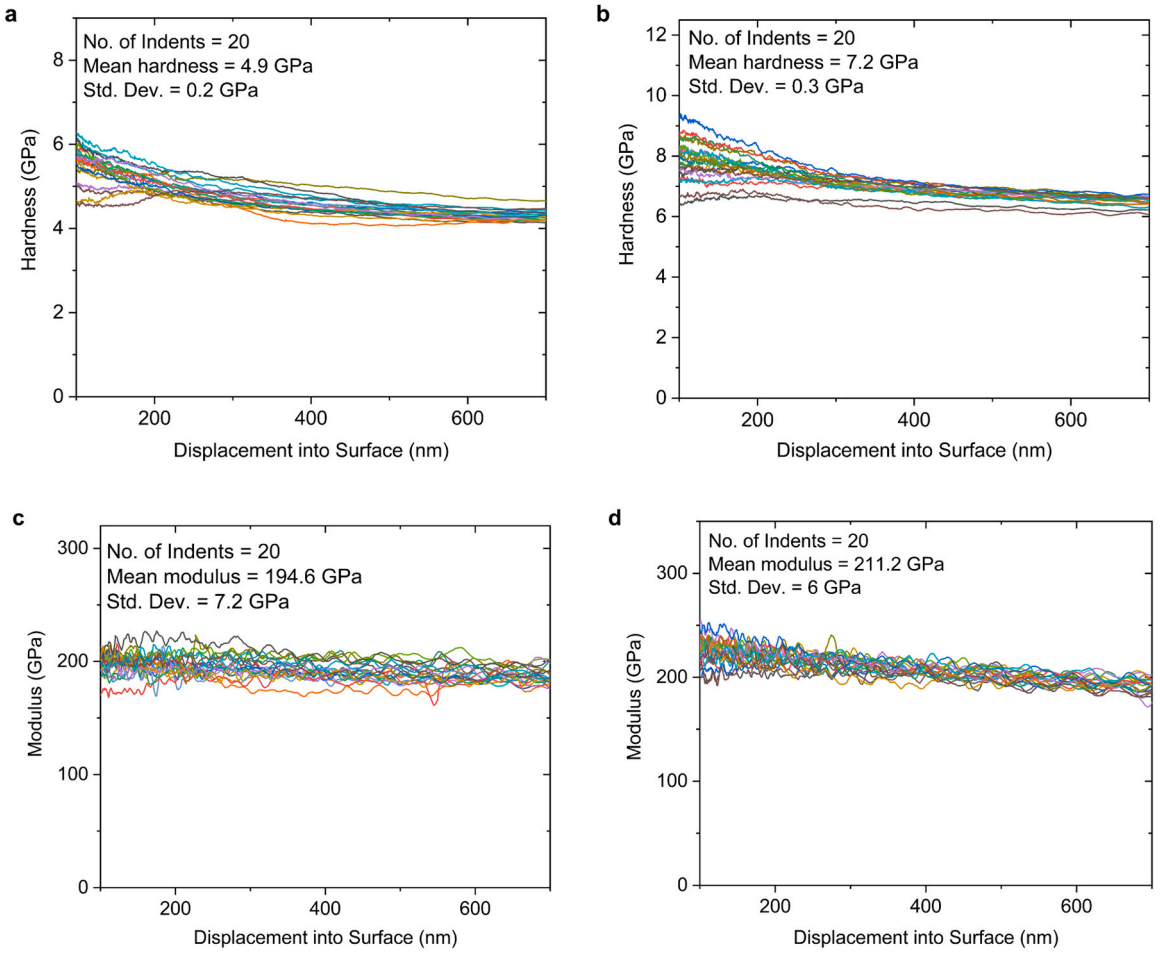


**Fig. 6.** Continuous stiffness measurement (CSM) hardness data from 20 indents, displaying the mean hardness value of **(a)** 4.9 GPa for EHEA2 * and **(b)** 7.2 GPa for EHEA3 * . Continuous stiffness measurement modulus data from 20 indents, showing the mean modulus value of **(c)** 194.6 GPa for EHEA2 * and **(d)** 211.2 GPa for EHEA3 * .

σ-phase. σ-phase is very hard and brittle, and it can significantly change the mechanical properties of the alloy. The formation of a σ-phase in $Al_5Cr_{32}Fe_{35}Ni_{22}Ti_6$ significantly increases the alloy's hardness from HV481 to HV950 but reduces its fracture toughness [35]. Additionally, the σ-phase is known to decrease the tensile ductility of HEAs [36,37]. Despite these drawbacks, the σ-phase offers distinct advantages in certain applications. Alloys with high σ-phase fractions demonstrate exceptional resistance to thermal softening, making them suitable for high-temperature environments [38]. Furthermore, the σ-phase can serve as a surface protection layer with excellent wear resistance, enhancing the material's performance in demanding environments [39].

Both our EHEA2 * and EHEA3 * samples have only 6 % σ-phase, which is a small amount compared to B2 and $L1_2$ phases. EHEA3 * contains 40 % B2 phase where as EHEA2 * contains 32 % B2 phase. This increased proportion of the B2 phase in EHEA3 * directly correlates with its superior hardness, as corroborated by nanoindentation results where EHEA3 * has higher hardness than EHEA2 * . The B2 phase is characterized by a simple cubic structure with alternating atom types, contributing to its higher symmetry and stronger atomic interactions. This ordered phase formation in high-entropy alloys (HEAs) exhibits higher atomic bonding strength than other phases. The presence of ordered structures in the B2 phase restricts dislocation movement, thereby

enhancing strength in HEAs. The ordered nature of the B2 phase makes dislocation motion more challenging because partial dislocations would disrupt the order of the structure. Restoring this order necessitates the coordinated movement of multiple dislocations, known as super-dislocations. Consequently, the requirement for dislocations to move in pairs rather than individually increases resistance to deformation [40–42]. The B2 phase can show a strong positive correlation with hardness due to several factors, including its lower atomic packing density, enhanced solid solubility, and reduced number of slip planes. These attributes highlight the critical role of the B2 phase in improving the hardness of HEAs and directly correlate with the higher hardness in EHEA3 * , which has a higher B2 phase than EHEA2 * .

In contrast, the deformation mechanism of the $L1_2$ phase is primarily influenced by dislocation slip and twinning. Recent studies have shown that the $L1_2$ phase can accommodate several arrays of parallel mobile dislocations and deform via planar slip [43]. The higher number of slip planes in the $L1_2$ phase allows it to deform more readily under load, contributing to its ductility. This distinction underscores the complementary roles of the B2 and $L1_2$ phases in tailoring the mechanical properties of high-entropy alloys. The B2 phase enhances strength and hardness, while the $L1_2$ phase contributes to improved ductility.

In addition to these phase-related observations, our previous research into the tensile properties of the EHEA $AlCoCrFeNi_{2.1}$ has shown that EHEA3 exhibits superior mechanical performance compared to other EHEAs and demonstrates higher yield strength and ultimate tensile strength [16]. The increased hardness of EHEA3 can be attributed to the unchanged presence of precipitates, stable nanolamellar spacing, and the retention of printing-induced pre-existing dislocation density. In contrast, the lower hardness of EHEA2 results from the absence of precipitates, the annihilation of dislocations, partial recrystallization, and the coarsening of nanolamellar spacing [16].

Interestingly, even before the melting process, EHEA3 exhibited higher yield strength, and following recrystallization, EHEA3 * consistently showed higher hardness than EHEA2 * . These observations suggest that the EHEA3 * sample retains a "memory" of its mechanical properties, which indicates its microstructure's stability and resilience. The term "memory retention" in this study refers to the observed stability of the hierarchical nanolamellar structure and dual-phase arrangement (B2 and $L1_2$) in EHEA samples after HPHT processing, specifically in the context of melting and recrystallization. While the microstructural stability and phase retention of HEAs under extreme conditions have been well-documented in the literature, this study expands on these findings by demonstrating that the EHEA samples not only retain their structural features but also undergo complete melting and recrystallization while preserving their nanolamellar characteristics. During the HPHT treatment, the samples underwent complete melting and subsequent recrystallization within the Paris-Edinburgh (PE) cell. Despite undergoing complete melting and reforming as a new sample, the alloy retained its B2 and $L1_2$ phases along with its nanolamellar morphology post-recrystallization. Notably, the lamellae remained in the nanoscale range rather than coarsening into the micrometer or sub-micrometer regime typically seen in conventional processing.

This remarkable structural preservation suggests a form of microstructural memory retention, where the material re-establishes its original nanostructure upon recrystallization. This unique observation of phase and nanostructure preservation post-recrystallization represents a novel phenomenon that has not been explicitly explored in the context of HPHT conditions, thereby contributing valuable insights into the behavior of EHEAs under such extreme environments.

The implications of this memory retention behavior are profound, as it provides new insights into the fundamental properties of high-ntropy alloys and their potential for use in advanced engineering applications.

## 5. Conclusions

In summary, as-printed EHEA1 $AlCoCrFeNi_{2.1}$ samples were synthesized through L-PBF and then annealed at $1000^0$ C for an hour (EHEA2), while the other was at $600^0$ C for five hours (EHEA3). Both samples were studied in extreme environments under high pressure and high temperature at the Advanced Photon Source at Argonne National Lab utilizing the Paris-Edinburgh press. EDXRD confirms that EHEA2 and EHEA3 samples have BCC and FCC phases. Melting of EHEA2 and EHEA3 samples was observed at $1698 \pm 25$ K and $1598 \pm 25$ K, respectively. The recrystallized EHEA2 and EHEA3 samples were recovered after melting, and the XRD of the recrystallized samples exhibited B2(BCC), $L1_2$(FCC), and σ phase. The recrystallized EHEA2 * and EHE3 * samples retain the memory of the annealed EHEA2 and EHEA3 samples. The nanoindentation hardness values of the EHEA2 * and EHEA3 * samples are 4.9 GPa and 7.2 GPa, and the nanoindentation modulus values of the EHEA2 * and EHEA3 * are 195 GPa and 211 GPa. We correlate the higher hardness values for EHEA3 * sample to higher content of the B2 phase. The Pressure-Volute-Temperature data reveals higher bulk modulus values for the BCC phase in both EHEA2 and EHEA3.

## CRediT authorship contribution statement

**Ren Jie:** Writing – review & editing, Methodology, Investigation, Formal analysis. **Rangari Vijaya:** Writing – review & editing, Investigation. **Yadav Abhinav:** Writing – review & editing, Investigation. **Yang Wuxian:** Writing – review & editing, Methodology, Investigation, Formal analysis. **Chen Wen:** Writing – review & editing, Methodology, Investigation, Funding acquisition, Conceptualization. **Vohra Yogesh K.:** Writing – review & editing, Supervision, Project administration, Funding acquisition, Conceptualization. **Chakrabarty Kallol:** Writing – review & editing, Writing – original draft, Methodology, Investigation, Formal analysis, Data curation. **Pope Andrew D.:** Writing – original draft, Methodology, Investigation, Formal analysis, Data curation.

## Declaration of Competing Interest

The authors declare that they have no conflict of interest.

## Acknowledgments

This material is based upon work supported by the Department of Energy-National Nuclear Security Administration Center of Excellence CAMCSE under Award Number DE-NA0004154. Portions of this work were performed at HPCAT (Sector 16), Advanced Photon Source (APS), Argonne National Laboratory. HPCAT operations are supported by DOE-NNSA's Office of Experimental Sciences. The Advanced Photon Source is a U.S. Department of Energy (DOE) Office of Science User Facility operated for the DOE Office of Science by Argonne National Laboratory under Contract No. DE-AC02–06CH11357. W.C. also acknowledges support from the National Science Foundation (DMR-2238204). Neutron diffraction studies were conducted at the Oak Ridge National Laboratory.

## Appendix A. Supporting information

Supplementary data associated with this article can be found in the online version at doi:10.1016/j.jallcom.2025.179470.

## Data Availability

Data will be made available on request.The data that support the findings of this study are available from the corresponding author upon reasonable request.

## References


[1] S. Kumar, Comprehensive review on high entropy alloy-based coating, Surf. Coat. Technol. 477 (2024) 130327.
[2] S.A. Krishna, N. Noble, N. Radhika, B. Saleh, A comprehensive review on advances in high entropy alloys: Fabrication and surface modification methods, properties, applications, and future prospects, J. Manuf. Process. 109 (2024) 583–606.
[3] Y.F. Ye, Q. Wang, J. Lu, C.T. Liu, Y. Yang, High-entropy alloy: challenges and prospects, Mater. Today 19 (2016) 349–362.
[4] Y. Zhang, T.T. Zuo, Z. Tang, M.C. Gao, K.A. Dahmen, P.K. Liaw, Z.P. Lu, Microstructures and properties of high-entropy alloys, Prog. Mater. Sci. 61 (2014) 1–93.
[5] B. Yin, F. Maresca, W.A. Curtin, Vanadium is an optimal element for strengthening in both fcc and bcc high-entropy alloys, Acta Mater. 188 (2020) 486–491.
[6] J. Dąbrowa, G. Cieślak, M. Stygar, K. Mroczka, K. Berent, T. Kulik, M. Danielewski, Influence of Cu content on high temperature oxidation behavior of AlCoCrCuxFeNi high entropy alloys (x = 0; 0.5; 1), Intermetallics 84 (2017) 52–61.
[7] J. Lu, Y. Chen, H. Zhang, L. Li, L. Fu, X. Zhao, F. Guo, P. Xiao, Effect of Al content on the oxidation behavior of Y/Hf-doped AlCoCrFeNi high-entropy alloy, Corros. Sci. 170 (2020) 108691.
[8] M.J. Yao, K.G. Pradeep, C.C. Tasan, D. Raabe, A novel, single phase, non-equiatomic FeMnNiCoCr high-entropy alloy with exceptional phase stability and tensile ductility, Scr. Mater. 72 (73) (2014) 5–8.
[9] D.B. Miracle, O.N. Senkov, A critical review of high entropy alloys and related concepts, Acta Mater. 122 (2017) 448–511.
[10] Y. Liao, I. Baker, Microstructure and room-temperature mechanical properties of Fe30Ni20Mn35Al15, Mater. Charact. 59 (2008) 1546–1549.
[11] Y. Liao, I. Baker, Evolution of the microstructure and mechanical properties of eutectic Fe30Ni20Mn35Al15, J. Mater. Sci. 46 (2011) 2009–2017.
[12] F. Meng, J. Qiu, I. Baker, Effect of Al content on the microstructure and mechanical behavior of two-phase FeNiMnAl alloys, J. Mater. Sci. 49 (2013) 1973–1983.
[13] J. Liu, Z. Li, D. Lin, Z. Tang, X. Song, P. He, S. Zhang, H. Bian, W. Fu, Y. Song, Eutectic high-entropy alloys and their applications in materials processing engineering: A review, J. Mater. Sci. Technol. 189 (2024) 211–246.
[14] Y. Lu, Y. Dong, S. Guo, L. Jiang, H. Kang, T. Wang, B. Wen, Z. Wang, J. Jie, Z. Cao, H. Ruan, T. Li, A promising new class of high-temperature alloys: eutectic high-entropy alloys, Sci. Rep. 4 (2014) 6200.
[15] Y. Lu, Y. Dong, H. Jiang, Z. Wang, Z. Cao, S. Guo, T. Wang, T. Li, P.K. Liaw, Promising properties and future trend of eutectic high entropy alloys, Scr. Mater. 187 (2020) 202–209.
[16] J. Ren, Y. Zhang, D. Zhao, Y. Chen, S. Guan, Y. Liu, L. Liu, S. Peng, F. Kong, J. D. Poplawsky, G. Gao, T. Voisin, K. An, Y.M. Wang, K.Y. Xie, T. Zhu, W. Chen, Strong yet ductile nanolamellar high-entropy alloys by additive manufacturing, Nature 608 (2022) 62–68.
[17] Y. Guo, H. Su, H. Gao, Z. Shen, P. Yang, Y. Liu, D. Zhao, Z. Zhang, M. Guo, Insight into annealing-induced hardening and softening behaviors in a laser powder-bed fusion printed in-situ composite eutectic high-entropy alloy, Compos. Part B: Eng. 281 (2024) 111523.
[18] P. Shi, W. Ren, T. Zheng, Z. Ren, X. Hou, J. Peng, P. Hu, Y. Gao, Y. Zhong, P. K. Liaw, Enhanced strength-ductility synergy in ultrafine-grained eutectic high-entropy alloys by inheriting microstructural lamellae, Nat. Commun. 10 (2019) 489.
[19] T. Bhattacharjee, I.S. Wani, S. Sheikh, I.T. Clark, T. Okawa, S. Guo, P. P. Bhattacharjee, N. Tsuji, Simultaneous Strength-Ductility Enhancement of a Nano-Lamellar AlCoCrFeNi(2.1) Eutectic High Entropy Alloy by Cryo-Rolling and Annealing, Sci. Rep. 8 (2018) 3276.
[20] X. Wang, G. Zhu, J. Liu, A. Zhang, H. Hou, Y.P. Zhang, H. Du, Microstructural stability and properties of Al1.2CrCuFeNi2 dual-phase high entropy alloy, Mater. Lett. 338 (2023) 134052.
[21] M. Wang, Y. Lu, J. Lan, T. Wang, C. Zhang, Z. Cao, T. Li, P.K. Liaw, Lightweight, ultrastrong and high thermal-stable eutectic high-entropy alloys for elevated-temperature applications, Acta Mater. 248 (2023) 118806.
[22] D. Herzog, V. Seyda, E. Wycisk, C. Emmelmann, Additive manufacturing of metals, Acta Mater. 117 (2016) 371–392.
[23] S. Gorsse, C. Hutchinson, M. Goune, R. Banerjee, Additive manufacturing of metals: a brief review of the characteristic microstructures and properties of steels, Ti-6Al-4V and high-entropy alloys, Sci. Technol. Adv. Mater. 18 (2017) 584–610.
[24] T. DebRoy, H.L. Wei, J.S. Zuback, T. Mukherjee, J.W. Elmer, J.O. Milewski, A. M. Beese, A. Wilson-Heid, A. De, W. Zhang, Additive manufacturing of metallic components – Process, structure and properties, Prog. Mater. Sci. 92 (2018) 112–224.
[25] Y.M. Wang, T. Voisin, J.T. McKeown, J. Ye, N.P. Calta, Z. Li, Z. Zeng, Y. Zhang, W. Chen, T.T. Roehling, R.T. Ott, M.K. Santala, P.J. Depond, M.J. Matthews, A. V. Hamza, T. Zhu, Additively manufactured hierarchical stainless steels with high strength and ductility, Nat. Mater. 17 (2018) 63–71.
[26] Z. Geng, C. Chen, R. Li, J. Luo, K. Zhou, Composition inhomogeneity reduces cracking susceptibility in additively manufactured AlCoCrFeNi2.1 eutectic high-entropy alloy produced by laser powder bed fusion, Addit. Manuf. 56 (2022) 102941.
[27] J. Ren, M. Wu, C. Li, S. Guan, J. Dong, J.-B. Forien, T. Li, K.S. Shanks, D. Yu, Y. Chen, K. An, K.Y. Xie, W. Chen, T. Voisin, W. Chen, Deformation mechanisms in an additively manufactured dual-phase eutectic high-entropy alloy, Acta Mater. 257 (2023) 119179.
[28] K. Katagiri, S.J. Irvine, A. Hari, R. Kodama, N. Ozaki, T. Sano, J. Ren, W. Yang, W. Chen, M.P. Clay, A.D. Pope, S. Iwan, L.E. Dresselhaus-Marais, Y.K. Vohra, Static and shock compression studies of eutectic high-entropy alloy AlCoCrFeNi2.1 to ultrahigh pressures, J. Appl. Phys. 135 (2024).
[29] Y. Kono, T. Irifune, Y. Higo, T. Inoue, A. Barnhoorn, P□V□T relation of MgO derived by simultaneous elastic wave velocity and in situ X-ray measurements: A new pressure scale for the mantle transition region, Phys. Earth Planet. Inter. 183 (2010) 196–211.
[30] B.H. Toby, R.B. Von Dreele, GSAS-II: the genesis of a modern open-source all purpose crystallography software package, J. Appl. Crystallogr. 46 (2013) 544–549.
[31] J. Gonzalez-Platas, M. Alvaro, F. Nestola, R. Angel, EosFit7-GUI: a new graphical user interface for equation of state calculations, analyses and teaching, J. Appl. Crystallogr. 49 (2016) 1377–1382.
[32] K. Tanaka, T. Saito, M. Yasuda, Soft X-ray emission spectra of aluminium in β-Phase Cu–Ni–Al and Cu–Mn–Al alloys, J. Phys. Soc. Jpn. 52 (1983) 1718–1724.
[33] F.A. Mauer, R.G. Munro, G.J. Piermarini, S. Block, D.P. Dandekar, Compression studies of a nickel-based superalloy, MAR-M200, and of Ni3Al, J. Appl. Phys. 58 (1985) 3727–3730.
[34] G. Bergman, D.P. Shoemaker, The determination of the crystal structure of the σ phase in the iron–chromium and iron–molybdenum systems, Acta Crystallogr. 7 (1954) 857–865.
[35] C.W. Lin, M.H. Tsai, C.W. Tsai, J.W. Yeh, S.K. Chen, Microstructure and aging behaviour of Al5Cr32Fe35Ni22Ti6 high entropy alloy, Mater. Sci. Technol. 31 (2015) 1165–1170.
[36] N.D. Stepanov, D.G. Shaysultanov, G.A. Salishchev, M.A. Tikhonovsky, E. E. Oleynik, A.S. Tortika, O.N. Senkov, Effect of V content on microstructure and mechanical properties of the CoCrFeMnNiVx high entropy alloys, J. Alloy. Compd. 628 (2015) 170–185.
[37] A.J. Zaddach, R.O. Scattergood, C.C. Koch, Tensile properties of low-stacking fault energy high-entropy alloys, Mater. Sci. Eng.: A 636 (2015) 373–378.
[38] C.-Y. Hsu, C.-C. Juan, W.-R. Wang, T.-S. Sheu, J.-W. Yeh, S.-K. Chen, On the superior hot hardness and softening resistance of AlCoCrxFeMo0.5Ni high-entropy alloys, Mater. Sci. Eng.: A 528 (2011) 3581–3588.
[39] M.-H. Chuang, M.-H. Tsai, C.-W. Tsai, N.-H. Yang, S.-Y. Chang, J.-W. Yeh, S.-K. Chen, S.-J. Lin, Intrinsic surface hardening and precipitation kinetics of Al0.3CrFe1.5MnNi0.5 multi-component alloy, J. Alloy. Compd. 551 (2013) 12–18.
[40] A. Poonia, M. Kishor, K.P.R. Ayyagari, Designing of high entropy alloys with high hardness: a metaheuristic approach, Sci. Rep. 14 (2024) 7692.
[41] V. Hasannaeimi, A.V. Ayyagari, S. Muskeri, R. Salloom, S. Mukherjee, Surface degradation mechanisms in a eutectic high entropy alloy at microstructural length-scales and correlation with phase-specific work function, npj Mater. Degrad. 3 (2019).
[42] Q. Wang, Y. Ma, B. Jiang, X. Li, Y. Shi, C. Dong, P.K. Liaw, A cuboidal B2 nanoprecipitation-enhanced body-centered-cubic alloy Al0.7CoCrFe2Ni with prominent tensile properties, Scr. Mater. 120 (2016) 85–89.
[43] S. Muskeri, V. Hasannaeimi, R. Salloom, M. Sadeghilaridjani, S. Mukherjee, Small-scale mechanical behavior of a eutectic high entropy alloy, Sci. Rep. 10 (2020) 2669.